

## Supplementary Information: Sodiation energetics in pore size controlled hard carbons determined via entropy profiling

### 1 Galvanostatic data at variable cycle rate

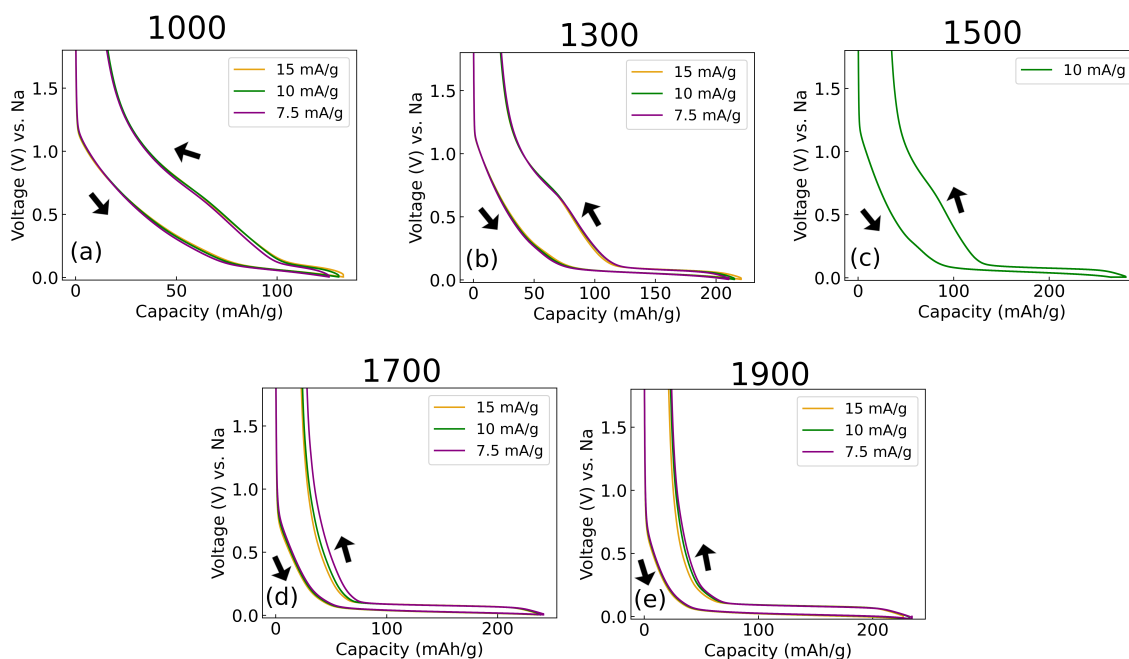


Figure S1: Galvanostatic data performed at the cycle rate indicated in the legend. In all cases, the second galvanostatic cycle at each C-rate is shown. The synthesis temperature of the hard carbon, in °C, is indicated at the top of each figure. (a)  $T_{\text{synth}} = 1000^{\circ}\text{C}$ , (b)  $T_{\text{synth}} = 1300^{\circ}\text{C}$ , (c)  $T_{\text{synth}} = 1500^{\circ}\text{C}$ , (d)  $T_{\text{synth}} = 1700^{\circ}\text{C}$ , (e)  $T_{\text{synth}} = 1900^{\circ}\text{C}$ . Arrows indicate cycle direction.

### 2 Comparison of cyclic voltammetry and dQ/dV

Results comparing slow rate cyclic voltammetry (CV) at scan rate 0.1 mV/s (from ref [1]), with dQ/dV from the present work are presented in Figure S2. dQ/dV obtained by the usual method of differentiating galvanostatic data are shown in Figure S2g; results from differentiating the entropy profile data (a form of GITT) are presented in Figure S2h. The CV results of the second scan are overlaid in Figure S2f, obtained from materials at different synthesis temperature. The cathodic (sodiation) scan shows a broad feature for all the studied hard carbons; whereas the anodic (desodiation) scan indicates well resolved peaks. This result indicates that the process of sodiation is kinetically limited at the 0.1 mV/s scan rate.

In contrast, dQ/dV obtained from 10 mA/g galvanostatic cycling shows clearly resolved peaks during sodiation and during desodiation. This trend is faithfully replicated in the dQ/dV data obtained from entropy profiling, which show nearly identical peak positions and widths to the galvanostatic data. However, the sodiation peak is still broader than that of the desodiation peak, and (with the exception of the  $T_{\text{synth}} = 1000^{\circ}\text{C}$  sample) the two peaks show a potential offset. The potential offset between the sodiation/desodiation peaks increases systematically with the sample synthesis temperature.

The poorly resolved sodiation peaks obtained from slow rate CV compared to dQ/dV can be explained as follows. In galvanostatic experiments, the polarisation resistance ( $iR$  drop) can be treated as a constant voltage offset because the current  $i$  is, by definition, constant, and the low frequency resistance contribution  $R$

varies insignificantly over the plateau region [2]. Therefore, when taking the derivative to obtain  $dQ/dV$ , the peak shape is unaffected by the  $iR$  drop. In contrast, the  $iR$  drop contribution changes dynamically in a CV experiment, because the current,  $i$ , varies, and is highest at the peaks. This leads to peak broadening as observed in the data shown here, with more severe broadening at higher sweep rates. This difference is particularly severe for the materials synthesised at higher synthesis temperature:  $T_{\text{synth}} = 1700^\circ\text{C}$  and  $T_{\text{synth}} = 1900^\circ\text{C}$ .

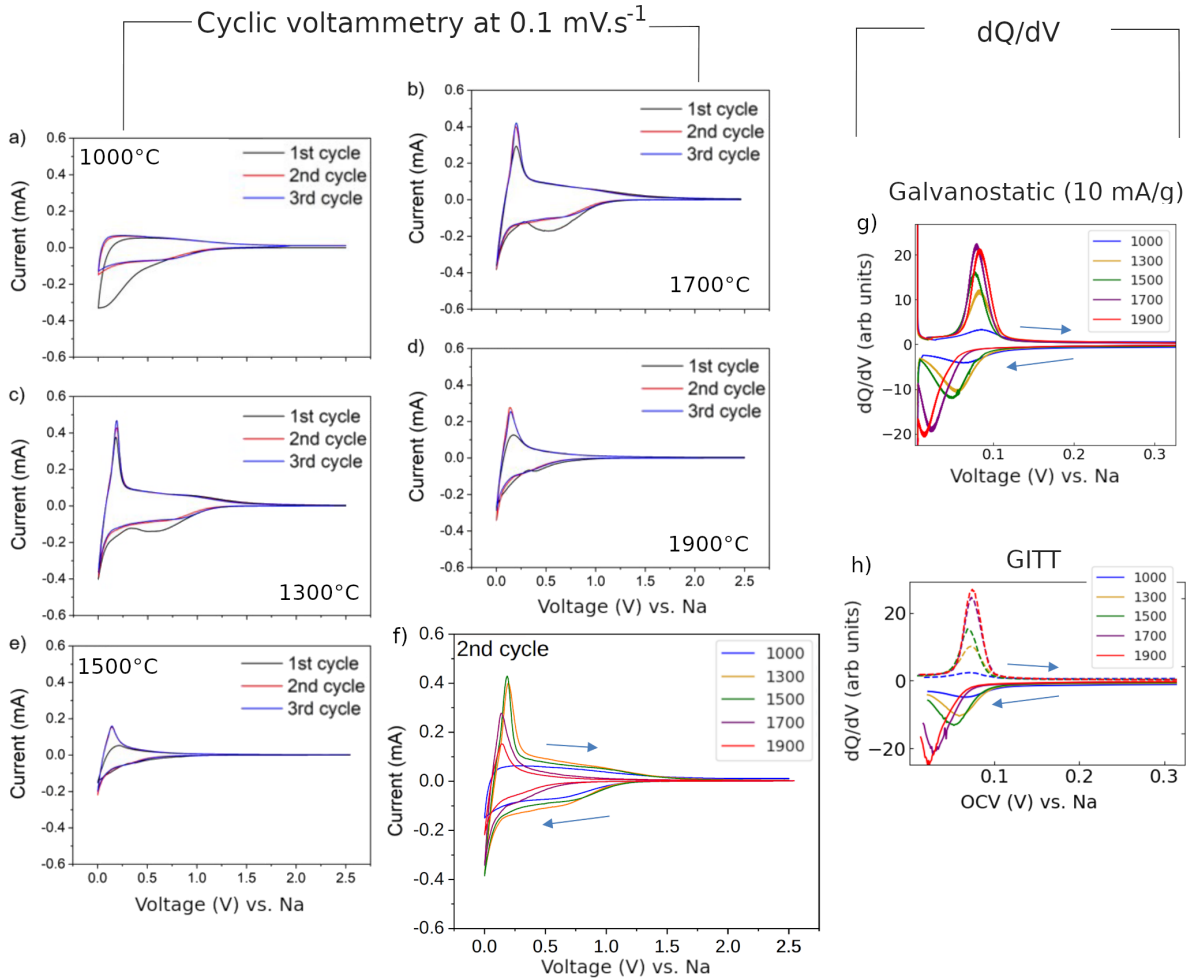


Figure S2: Comparison of results from slow rate cyclic voltammetry (CV) (a-f) with results from  $dQ/dV$ . CV data at a scan rate of  $0.1 \text{ mV/s}$  (a-e) were obtained (adapted) from Figure S8 of ref. [1], where the synthesis temperature is indicated in each panel. The results from the second galvanostatic cycle are overlaid at each synthesis temperature. (g)  $dQ/dV$  results, obtained from the second galvanostatic cycle at  $10 \text{ mA/g}$  (corresponding to results presented in Figure S1). (h)  $dQ/dV$  results obtained from the entropy profiling method shown in the main paper.

### 3 Optimisation procedure

We utilised the optimisation procedure from our previous work [3] to fit the simulated parameters,  $\theta$ , in the Bragg-Williams (BW) model to multiple experimental curves. The following method was applied to all five hard carbons examined in the study, with at least 3 repeat experimental measurements performed on each. To check the robustness of the optimisation procedure, the method below was repeated on each data set at least 3 times. Very similar parameters resulted from repeat runs of the optimisation procedure, indicating a robust method.

The curves of interest were the experimental OCV, the enthalpy and entropy profiles  $dH/dx$  and  $dS/dx$ , respectively, and  $dQ/dV$ . We also found that fitting the derivatives of the enthalpy and entropy profiles, i.e.  $d^2H/dx^2$  and  $d^2S/dx^2$ , led to more robust optimisation.

The number of parameters,  $\theta$ , necessitated a multiple-stage optimisation process to consistently find valid solutions and reduce the risk of finding local minima. The three stages can be summarised as:

1. Minimise  $f(\theta)$ , a weighted sum of the root mean square (RMS) difference between the simulated and experimental curves (excluding  $dQ/dV$  with weight zero), using the particle swarm method. At this stage,  $\theta = [L, A, B, \epsilon_1, \Delta\epsilon, Q_{\max}, \Delta S_{\text{corr}}]$ .
2. Using initial parameter values determined from the previous stage, and the same arguments  $\theta$ , minimise  $f(\theta)$  with the Nelder-Mead simplex method.
3. Using initial parameter values determined from the previous stage,  $\theta = [L, A, B, \epsilon_1, \Delta\epsilon, Q_{\max}, \Delta S_{\text{corr}}, g_2]$ , and including  $dQ/dV$  in the fitting process, minimise  $f(\theta)$  with the Nelder-Mead simplex method.

The penalty function,  $f(\theta)$  is given by

$$f(\theta) = \underline{w} \cdot \underline{f}_{\text{var}}(\theta), \quad (\text{S1})$$

where the weights are  $\underline{w}$  and the individual functions are  $\underline{f}_{\text{var}}(\theta)$ .

The functions to be minimised are given by

$$\underline{f}_{\text{var}}(\theta) = [f_{\text{OCV}}(\theta), f_{\text{dH}}(\theta), f_{\text{dS}}(\theta), f_{\text{dQdV}}(\theta), f_{\text{d2H}}(\theta), f_{\text{d2S}}(\theta)], \quad (\text{S2})$$

where  $f_{\text{OCV}}(\theta)$ ,  $f_{\text{dH}}(\theta)$ ,  $f_{\text{dS}}(\theta)$ ,  $f_{\text{dQdV}}(\theta)$ ,  $f_{\text{d2H}}(\theta)$  and  $f_{\text{d2S}}(\theta)$  are the RMS errors obtained from simulated and experimental datasets. For example, the RMS error of the open circuit voltage, OCV is given by

$$f_{\text{OCV}}(\theta) = \frac{\sqrt{\sum_{i=1}^P (E_{\text{OCV},i}^{\text{sim}}(\theta) - E_{\text{OCV},i}^{\text{expt}})^2}}{P}, \quad (\text{S3})$$

where  $P$  represents the number of points obtained after 1D cubic interpolation of the simulated data points onto the experimental data grid (implemented using “interp1d” from the Scipy library),  $E_{\text{OCV},i}^{\text{sim}}(\theta)$  is the simulated OCV dependent on the input arguments, and  $E_{\text{OCV},i}^{\text{expt}}$  is the experimentally-measured OCV. The other functions that were minimised likewise were  $f_{\text{dH}}(\theta) : dH/dx$ ,  $f_{\text{dS}}(\theta) : dS/dx$ ,  $f_{\text{dQdV}}(\theta) : dQ/dV = -dx/dE_{\text{OCV}}$ ,  $f_{\text{d2H}}(\theta) : d^2H/dx^2$  (obtained by differentiation of equation 7 from the main paper),  $f_{\text{d2S}}(\theta) : d^2S/dx^2$  (obtained by differentiation of equation 6 from the main paper).

The weighting factors are

$$\underline{w} = [w_1, w_2, w_3, w_4, w_5, w_6], \quad (\text{S4})$$

where  $w_1$  through to  $w_6$  are empirical weighting factors for each dataset. Through trial and error, the most robust fitting during the particle swarm optimisation (numbered stage 1 above) was obtained by:  $w_1 = 1$ ,  $w_2 = 4$ ,  $w_3 = 4$ ,  $w_4 = 0.5$ ,  $w_5 = 0.5$ ,  $w_6 = 0$ , i.e.  $dQ/dV$  was initially excluded from the fitting process.

The particle swarm optimisation was implemented using the pyswarm module currently available at “<https://pythonhosted.org/pyswarm/>”. The following function arguments in “pso” were found to result in consistent solutions:  $\text{maxiter} = 200$ ,  $\text{swarmsize} = 400$ ,  $\text{minstep} = 5e-7$ ,  $\text{minfunc} = 5e-7$ . The velocities “omega”, “phip” and “phig” were all set to 0.75. The arguments during stages 1 and 2 were

$$\theta = [\phi, A, B, \epsilon_1, \Delta\epsilon, Q_{\max}, \Delta S_{\text{corr}}] \quad (\text{S5})$$

where the terms above are defined in Table 2 of the main paper. Results suggested that the theoretical maximum capacity,  $Q_{\max}$ , extended beyond the experimentally measured capacity, and hence the simulated data was rescaled according to a procedure detailed in section 4.  $\Delta S_{\text{corr}}$  is a constant correction factor to the partial molar entropy,  $\Delta S(x)$

$$\Delta S(x) = \frac{\partial S(x)}{\partial x} = \frac{\partial S_{\text{conf}}(x)}{\partial x} + \Delta S_{\text{corr}}, \quad (\text{S6})$$

where  $\Delta S_{\text{conf}}$  is the partial molar configurational entropy determined by solving the partition function,  $\Delta S_{\text{corr}}$  is a constant fitted parameter and  $\Delta S(x)$  includes all entropy contributions.

The particle swarm optimisation was applied to ensure more robust optimisation results dependent on the initial parameters,  $\theta$ . The method is stochastic, which means the results of the optimisation procedure might be different from one run to another. However, with the input arguments specified as above, it was found that consistent solutions were obtained from 3 independent runs of the procedure.

In stage 2, simulation results were refined using the Nelder-Mead simplex method. This was implemented using the “minimize” function from Scipy. The initial guess for the input parameters was determined from the result of the particle swarm optimisation (optimisation stage 1).

Lastly, in stage 3,  $w_6$  was set to 0.1 to include fitting of the  $dQ/dV$  data while leaving the other weighting factors unchanged. The number of input parameters was expanded to include  $g_2$ , i.e.

$$\theta = [\phi, A, B, \epsilon_1, \Delta\epsilon, Q_{\max}, \Delta S_{\text{corr}}, g_2], \quad (\text{S7})$$

with  $g_2$  initially set to zero and the remaining parameters were initialised using the results from the previous stage of optimisation. This final optimisation stage allowed the experimental dQ/dV peak FWHM and shape to be faithfully replicated, while resulting in only minor changes to the results of the other thermodynamic variables. The entire parameter set was then again fitted using the Nelder-Mead simplex method.

## 4 Comparing experimental and model concentrations

It is important to account for the sodium filling fractions used to derive the thermodynamic variables obtained from experiment and compare them consistently with modelled results.

It was found during the numerical optimisation procedure detailed in section 3 that the maximum theoretical capacity obtained from the fitting process,  $Q_{\max}$ , which corresponds to a maximum desodiation fraction of  $x = 1$ , was greater than the experimentally-determined maximum capacity,  $Q_{\text{expt}}$ . This finding indicates that there is in principle additional sodiation capacity below cell voltage -0.02 V versus Na. It also means that we must carefully consider the  $x$  scale of all thermodynamic variables differentiated with respect to  $x$ , as shown subsequently.

We have already defined  $x$  as the theoretical sodiation filling fraction in the model, where  $0 < x < 1$ . We assume that at minimum capacity, all sodium is removed from the lattice, because we initialised all thermodynamic measurements from a CCCV condition at 2.0 V versus Na. Therefore

$$x = \frac{Q}{Q_{\max}}, \quad (\text{S8})$$

where  $Q$  is the measured capacity obtained from experiment in mAh/g. We can similarly define

$$x_{\text{expt}} = \frac{Q}{Q_{\text{expt}}}, \quad (\text{S9})$$

where  $x_{\text{expt}}$  similarly goes from 0 to 1. However, with  $Q_{\max} \neq Q_{\text{expt}}$ , there is a conversion factor required to relate simulated and experimental data on an equivalent  $Q$  scale.

Let us now define  $k = Q_{\text{expt}}/Q_{\max}$ . In the fitting procedure in section 3, we made use of the second derivatives of  $H(x)$  and  $S(x)$  with respect to  $x$ . These must be written as

$$\frac{\partial^2 H(x)}{\partial x_{\text{expt}}^2} = k^2 \frac{\partial^2 H(x)}{\partial x^2}, \quad (\text{S10})$$

and likewise for  $S(x)$ .

For dQ/dV, the appropriate transformation is

$$\frac{dQ}{dV} = -\frac{dx_{\text{expt}}}{dE_{\text{OCV}}(x)} = -\frac{1}{k^2} \left( \frac{dx}{dE_{\text{OCV}}(x)} \right), \quad (\text{S11})$$

where the minus sign emerges because the measurement was performed by galvanostatic discharge.

## 5 Interaction parameters from Bragg-Williams model

The following interaction parameters were determined by fitting the Bragg-Williams model, as described in the main paper, to the experimental electrochemical thermodynamic data. The parameters are defined in Table S1.

Table S1: Energetic terms from the Bragg-Williams model, dependent on synthesis temperature  $T_{\text{synth}}$  ( $^{\circ}\text{C}$ ). The other interaction parameter,  $Q_{\max}$ , is presented in Table 4 of the main paper

$T_{\text{synth}}$ ( $^{\circ}\text{C}$ )	$\epsilon_1$ (meV)	$\epsilon_2$ (meV)	$g_2$ (meV)	$A$ (eV)	$B$	$\Delta S_{\text{corr}}$ ( $\text{J mol}^{-1} \text{K}^{-1}$ )	$\phi$
1000	-241	-58	8	-1.73	1.54	-0.67	0.682
1300	-318	-29	-8	-1.29	1.67	4.05	0.359
1500	-386	-5	-19	-2.04	2.19	9.29	0.393
1700	-173	10	-31	-0.79	1.90	3.42	0.278
1900	-61	15	-30	-0.36	1.04	3.72	0.238

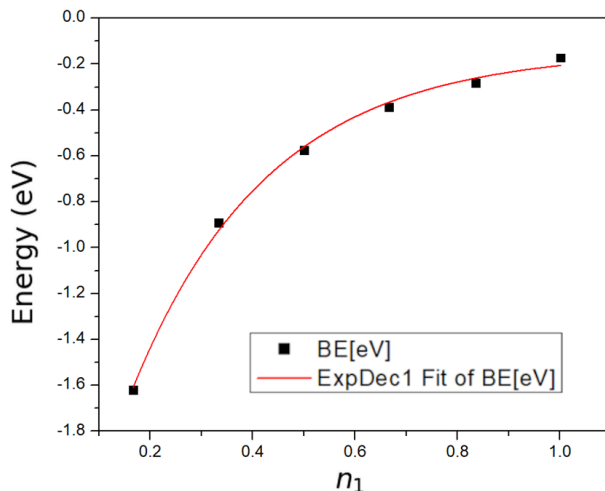


Figure S3: Black points: DFT data obtained from Figure 6 of ref. [11], for the binding energy (BE) of sodium adsorption on graphene. Data re-used with permission from Elsevier Ltd., Copyright 2018. The binding energy as a function of sodium concentration,  $n_1$  is obtained. The fitted function, obtained within the present work, is  $E = A\exp(-Bn_1) + y_0$ , where  $E$  is the adsorption energy of sodium on graphene. The fitting coefficients, obtained from least squares regression, were:  $y_0 = -0.143$  eV,  $A = -2.749$  eV,  $B = 3.765$ .

## 6 Physical explanation for interlayer interaction term

In the Bragg-Williams model, the term  $\epsilon'_1$  varies with sodiation fraction  $n_1$ , accounting for the ionic state of sodium in the interlayer filling region dependent on sodiation fraction. This is because when an alkali metal is intercalated into a compound with a low density of states (DOS) at the Fermi level, large changes in chemical potential occur, as highlighted by Dahn et al. [4]. This results in rapid changes of the point term of lithium in graphite at low lithium occupation, resulting in additional electrochemical features [5]. Similarly, the local structure of hard carbons approximates to curved bilayer graphene, which also presents a low DOS at the Fermi level [6, 7]. In fact, Stratford et al. found localised charge transfer between sodium and carbon defects in hard carbons by in-situ NMR [7]. They found changes in the local environment of the sodium ions with an increase in the amount of sodium in the hard carbon, implying that the sodium species become increasingly metallic as the voltage decreases. A greater Knight shift was obtained with increasing sodium concentration, indicating an increase of the Na 2s DOS at the Fermi level. The operando Raman measurements of Euchner et al. combined with DFT calculations of phonon spectra, suggest a downwards shift in the G-band through as more sodium is added in the sloping region [6], which was also observed experimentally by Weaving et al. [8]. Both groups attributed this shift to charge transfer from the metal atoms to the carbon matrix [6, 8]. DFT calculations combined with Bader charge transfer analysis also suggest changes in the charge transfer from sodium to carbon dependent on the amount of inserted sodium [9, 10, 11].

Based on arguments presented previously for lithium in graphite [5, 4, 12] and the experimental/DFT evidence for the sodium in hard carbon system, it is therefore reasonable to assume that the interlayer point term,  $\epsilon'_1$ , varies dependent on the sodiation fraction,  $n_1$ . This is in line with the DFT data of Wasalathilake et al. [11], who showed a more negative binding energy,  $\Delta E_{\text{Na}}$ , at low sodium occupation that decays to a less negative  $\Delta E_{\text{Na}}$  as the lattice becomes sodiated. We show DFT data from Wasalathilake et al. in Figure S3, for sodium adsorption on graphene.

Consistently with these calculations, we found that a relationship of the form

$$\epsilon'_1(n_1) = \epsilon_1 + A\exp(-Bn_1), \quad (\text{S12})$$

gave a satisfactory fit to the experimental results for the partial molar enthalpy variation in the sloping region. This is equivalent to equation 10 from the main paper, where the terms  $\epsilon_1$ ,  $A$  and  $B$  are defined. Pairwise Na-Na interactions were tested, but were found to negligibly influence the thermodynamic behaviour compared with the variation in Na-C interactions expressed in equation S12. Therefore, pairwise interactions were neglected. The quantitative values obtained for  $A$  and  $B$  by fitting the experimental thermodynamic profiles (c.f. Table S1) differ from those shown in Figure S3, which are based on DFT data [11]. Nevertheless, the experimental and DFT parameters are in qualitative agreement, with both parameter sets describing an exponentially decaying binding energy with the same sign and order of magnitude of the interaction. Quantitative differences between experiment and the model likely arise from the DFT exchange correlation functional, as well as planar graphene being an imperfect proxy system for hard carbon.

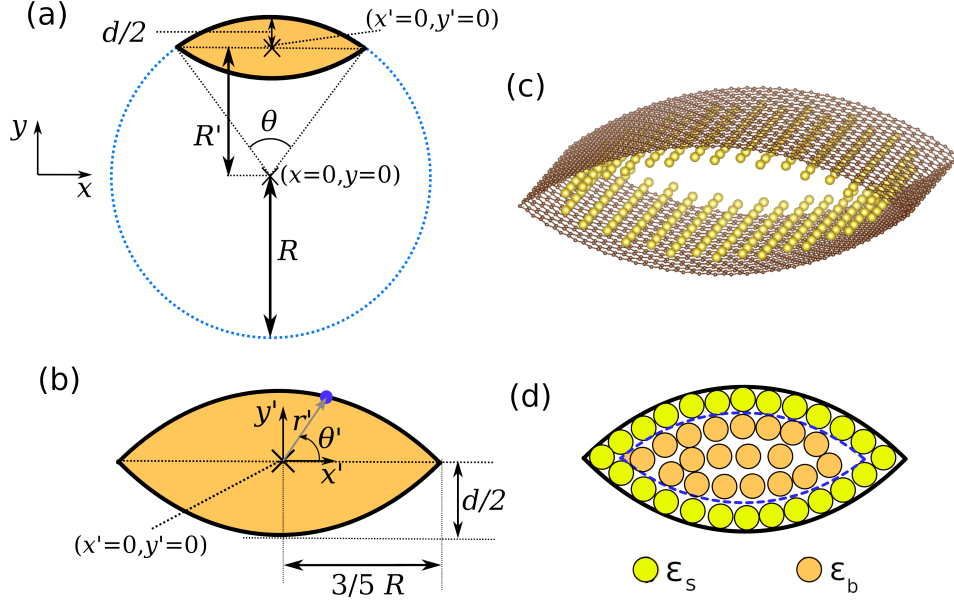


Figure S4: (a) The blue dotted line is the cross section of a cylinder. The orange area is enclosed between two curved graphene sheets, which are represented by black solid lines. The origin of the original Cartesian coordinate system  $(x, y)$  is shown. (b) Zoom in of the enclosed area. The origin in the translated Cartesian coordinate system  $(x', y')$  is shown. Any point along the cross section of the top graphene plane is defined in the polar system  $(r', \theta')$ , as shown by the blue point and blue arrow. (c) atomic scale visualisation of the system, with carbon atoms shown in brown. A monolayer of enclosed sodium atoms is shown in yellow. (d) Separation of nanopore sites into surface sites of energy  $\epsilon_s$  and interior sites of energy  $\epsilon_b$ .

## 7 Eyelid construction

Let us define a cylinder, radius  $R$ , of arbitrary length,  $L$ . The outline of this cylinder is given by

$$x^2 + y^2 = R^2 \quad (\text{S13})$$

where  $x$  and  $y$  are Cartesian coordinates with  $(x = 0, y = 0)$  defining the centre of the cylinder.

Part of this cylinder defines the outline of a graphene sheet. The cross section of the top graphene sheet is an arc. Stratford et al. [13] showed that all hard carbons produced by hydrothermal synthesis exhibited cylindrical curvature. Therefore, they hypothesised that the porous regions within hard carbon can be approximated by curved graphene sheets. If two such graphene sheets are on top of one another, they form a porous region shape of an ‘‘eyelid’’, as shown in Figure S4b. The construction is shown with atomically accurate coordinates in Figure S4c.

We can translate the Cartesian coordinate system to  $x', y'$ , such that  $(x' = 0, y' = 0)$  defines the centre of the eyelid. We then obtain by geometry

$$x' = x \quad (\text{S14})$$

$$y' = y - R' \quad (\text{S15})$$

where  $R' = R - \frac{1}{2}d$ , and  $d$  is the distance between the top and bottom of the eyelid.

From comparison of the average pore size obtained from small angle x-ray scattering (SAXS) and pair distribution function (PDF) analysis (see below for interpretation and discussion of the pore size discrepancy), we also know that  $d \approx \frac{2}{5}R$ . Hence

$$R' = \frac{4}{5}R \quad (\text{S16})$$

leading to

$$y' = y - \frac{4}{5}R. \quad (\text{S17})$$

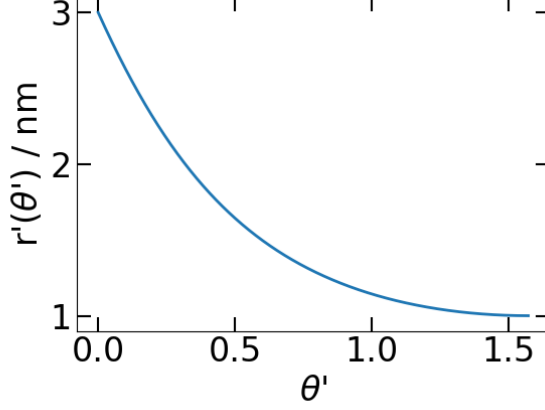


Figure S5: Plot of  $r'(\theta')$  as a function of  $\theta'$ , as defined in equation S23. Data are plotted over the interval  $0 \leq \theta' \leq \pi/2$ . The input value of  $R$  was 5 nm.

We can now define a polar coordinate system centred on  $(x' = 0, y' = 0)$ .  $r'$  defines the distance from this point,  $\theta'$  is the angle in radians. By the usual conventions,  $\theta' = \frac{\pi}{2}$  is along the  $y'$  and  $y$  axes while  $\theta' = 0$  lies along the  $x'$  axis. The coordinate system is shown explicitly in Figure S4b. Hence

$$x' = r' \cos(\theta') \quad (\text{S18})$$

$$y' = r' \sin(\theta'). \quad (\text{S19})$$

Rearranging the above, we can obtain

$$(y' + R)^2 + x'^2 = R^2. \quad (\text{S20})$$

Through further rearrangement (taking note of the identity  $\sin^2(\theta') + \cos^2(\theta') = 1$ ), we eventually get

$$r'^2 + \frac{8}{5}Rr' \sin(\theta') = \frac{9}{25}R^2. \quad (\text{S21})$$

We can solve this quadratic equation to get  $r'(\theta')$ . Applying the usual formula for solution of a quadratic, and taking the positive square root (resulting in the only positive solution for  $r'(\theta')$ ), it is found that

$$r'(\theta') = -\frac{4}{5}R \sin(\theta') + \frac{R}{10} \sqrt{64 \sin^2(\theta') + 36}, \quad (\text{S22})$$

which has the following, slightly simpler form

$$r'(\theta') = \frac{R}{10} \left( \sqrt{64 \sin^2(\theta') + 36} - 8 \sin(\theta') \right). \quad (\text{S23})$$

We can validate this expression at select values of  $\theta'$ . At  $\theta' = 0$ ,  $r' = \frac{3}{5}R$ , while at  $\theta' = \frac{\pi}{2}$ ,  $r' = \frac{1}{5}R$ , as expected. It can also be seen from Figure S4b that the maximum value of  $r'$  corresponds to  $\theta' = 0$  (the ends of the graphene sheet), and  $r'$  decreases as the angle increases, with a minimum value of  $r'$  when  $\theta' = \frac{\pi}{2}$ .

The shape of this construction is not only consistent with the cylindrical curvature obtained from pair distribution function (PDF) analysis of synchrotron x-ray data [13], but also explains why there is a discrepancy between the average pore size obtained from small angle x-ray scattering (SAXS) and PDF measurements [13, 1] for hydrothermal carbons synthesised at the same temperature. It can be seen from Figure S4b that in the interval between  $\theta' = 0$  and  $\theta' = \frac{\pi}{2}$ ,  $r'$  does not decrease linearly with increasing  $\theta'$ , as shown in Figure S5.

We can also determine the average radius of the eyelid construction,  $r_{\text{avg}}$  using

$$r_{\text{avg}} = \frac{2}{\pi} \int_{\theta'=0}^{\theta'=\frac{\pi}{2}} r'(\theta') d\theta'. \quad (\text{S24})$$

Plugging in the result for  $r'(\theta')$  (equation S23) and solving the integral numerically yields a value of  $r_{\text{avg}} \approx 0.6d$ . The average diameter,  $d_{\text{avg}}$ , is therefore given by  $d_{\text{avg}} \approx 1.2d$ , i.e. slightly larger than the distance between the top and bottom of the eyelid. We think this average diameter is the most representative size probed by SAXS.

## 8 Derivation of surface and volume energy terms

Having described the model of the hard carbon substrate in terms of the eyelid model, we can now evaluate the energetics of sodiation inside the nanopores. The following is an extended version of sections 2.5.2 and section 3.4 presented in the main paper.

In a similar spirit to the BET isotherm, we treat the sodium deposition in two levels: surface and bulk-like (second layer and higher) sites. The surface sites are sodium atoms adsorbed to the curved carbon substrate, while the bulk-like sites represent sodium deposited either directly on to the surface sites or even further inside the pore.

Using the construction represented in Figure S4a, we can determine the total enclosed volume inside the pore,  $V_{\text{tot}}$ , and the total surface area of the top and bottom of the eyelid,  $S_{\text{tot}}$ .

The area of the shaded cross-section shown in Figure S4a is evaluated by subtracting the area of the isosceles triangle of angle  $\theta$  from the area of a sector of the same angle. The area of the resulting segment is then multiplied by 2 (and the arbitrary length,  $L$ ), to obtain  $V_{\text{tot}}$ . More formally

$$V_{\text{tot}} = LR^2(\theta - \sin(\theta)). \quad (\text{S25})$$

Likewise, the total arc length defines a cross-section, which when extruded along length  $L$ , forms a total area

$$S_{\text{tot}} = 2LR\theta. \quad (\text{S26})$$

From the dimensions shown in Figure S4a-b it is found that  $\theta \approx 1.29$  radians. With this, we can determine the energetics of sodium filling inside the nanopores. Based on the assumptions above, we split the energetics into a surface and a bulk-like term. When all of the available sites are filled with sodium, the total sodium adsorption energy  $E_{\text{Na}}$  is given by

$$E_{\text{Na}} = V_{\text{tot}}\rho_V\epsilon_b + S_{\text{tot}}\rho_s\epsilon_s \quad (\text{S27})$$

where  $\rho_V$  is the packing density of sodium in the bulk phase (in atoms per unit volume),  $\rho_s$  is the packing density of sodium in the surface layer (in atoms per unit area),  $\epsilon_b$  is the energy per site of sodium atoms in the bulk phase, and  $\epsilon_s$  is the energy per site of sodium atoms in the surface layer.

Through the geometrical arguments presented above, we can find that

$$E_{\text{Na}} = 0.329\rho_V\epsilon_bR^2L + 1.286\rho_s\epsilon_sRL. \quad (\text{S28})$$

We can then divide through by the number of bulk atoms to obtain

$$\frac{E_{\text{Na}}}{0.329\rho_VR^2L} = \epsilon_b + \frac{3.91\rho_s\epsilon_s}{\rho_VR}. \quad (\text{S29})$$

If the number of bulk Na atoms is much larger than the number of interface Na atoms, we can assimilate the first term into an average binding energy per site,  $\epsilon'_2$ . Thus

$$\epsilon'_2 = \epsilon_b + \frac{3.91\rho_s\epsilon_s}{\rho_VR}. \quad (\text{S30})$$

We can make certain assumptions to obtain  $\rho_s$  and  $\rho_V$ . For  $\rho_V$ , we assume the bulk body-centred cubic packing density of  $\rho_V = 25.5$  atoms  $\text{nm}^{-3}$ . The lowest energy surface of Na is (110), which has a packing density of  $\rho_s = 7.7$  atoms  $\text{nm}^{-2}$ . The only unknowns in equation S30 are then  $\epsilon_b$  and  $\epsilon_s$ , which can be obtained by plotting  $\epsilon'_2$  as a function of the apparent size from SAXS,  $r_{\text{avg}}$ , as shown in Figure S6b.

Given that this relationship applies when all of the sodium sites are occupied, we can utilise the term  $\epsilon'_2$  defined within the Bragg-Williams (BW) model in the main paper and take the nanopore sublattice occupancy,  $n_2 = 1$ . Based on the point term,  $\epsilon_2$ , and Frumkin interaction parameter  $g_2$ , each obtained from fitting the BW model to the experimental thermodynamic profiles, we find  $\epsilon'_2 = \epsilon_2 + g_2$ . The relationship shown in Figure S6b is found to be of the form  $y = mx + c$  and the parameters obtained from linear regression are indicated in Figure S6b.

From the linear regression fit,  $\epsilon_b = -0.0045$  eV. It is reasonable to approximate  $\epsilon_b \approx 0$  eV, and therefore the bulk term co-incides with the onset of bulk sodium deposition at 0 V vs. Na.

It is informative to estimate how the radius determined from SAXS,  $r_{\text{SAXS}}$  relates to  $R$ . A crude approximation is to take  $r_{\text{SAXS}} \approx d/2 = r = R/5$ , where  $d$  is shown in Figure S4b. However, to account for the different ways that x-rays can be scattered in a porous structure, a more realistic approximation is that  $r_{\text{SAXS}} = r_{\text{avg}}$ , which was defined in equation S24, i.e.  $r_{\text{avg}} \approx 0.6d = 0.24R$ . In this case,  $r$  is slightly smaller than  $r_{\text{avg}}$ , as shown in the values in Table S2.

Substituting the SAXS radius  $r_{\text{SAXS}} = r_{\text{avg}}$  into equation S30, we obtain

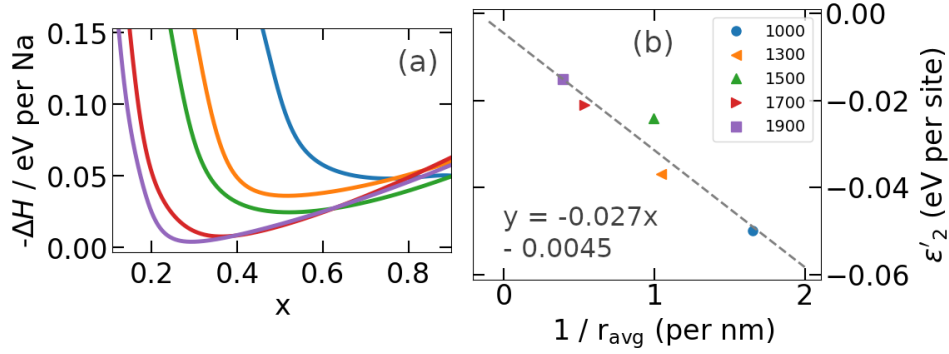


Figure S6: (a) simulated partial molar enthalpy as function of sodium concentration  $x$  (as previously shown in the main paper). (b) nanopore energy term  $\epsilon'_2$  as a function of  $1/r_{\text{avg}}$ , where  $r_{\text{avg}}$  is the nanopore radius determined from small-angle x-ray scattering (SAXS). The legend refers to the pyrolysis temperature of each respective hard carbon.

Table S2: Dimensional and energetic data of hard carbons.  $T_{\text{synth}}$  is the synthesis temperature,  $\epsilon'_2$  (eV) is the average energy per atom of the sodium sites,  $d$  is the minimum distance between the top and bottom of the eyelid shown in Figure S4b,  $r_{\text{avg}}$  is the average radius determined in equation S24, assumed to be the size probed by SAXS and  $R$  is the radius of curvature determined by PDF analysis[13]

$T_{\text{synth}}$ (°C)	$\epsilon'_2$ (eV)	$r = d/2$ (nm)	$r_{\text{avg}}$ (nm)	$R$ (nm)
1000	-0.050	0.51	0.61	3.0
1300	-0.037	0.80	0.96	4.8
1500	-0.024	0.84	1.01	5.0
1700	-0.021	1.55	1.86	9.3
1900	-0.015	2.13	2.56	12.8

$$\epsilon'_2 = \epsilon_b + \frac{0.938\rho_s\epsilon_s}{\rho_V r_{\text{avg}}}. \quad (\text{S31})$$

With  $r_{\text{SAXS}} = r_{\text{avg}}$ , inserting the linear regression fit parameters from Figure S6b into equation S30, it is found that

$$-0.027 = \frac{0.938\rho_s\epsilon_s}{\rho_V}, \quad (\text{S32})$$

and hence a numerical value of  $\epsilon_s = -0.095$  eV is obtained. Therefore, the curvature of the pore makes sodium deposition on the pore walls energetically favourable.

## 9 Nanopore energetics for cylindrical pores

In the case of a pore comprised of three or more graphene layers, the pore would be expected to approximate to a cylinder of radius  $R$ . Equation S27 is also applicable in this case.

Performing analysis similar to the previous section, we can substitute  $V_{\text{tot}} = \pi R^2 L$  and  $S_{\text{tot}} = 2\pi RL$  (note: the ends of the cylinder are assumed to be open) and obtain

$$E_{\text{Na}} = \pi R^2 L \rho_V \epsilon_b + 2\pi RL \rho_S \epsilon_s. \quad (\text{S33})$$

Rearranging similar to before, we obtain

$$\frac{E_{\text{Na}}}{\pi R^2 L \rho_V} = \epsilon_b + \frac{2\rho_S \epsilon_s}{R \rho_V}, \quad (\text{S34})$$

and, by the reasoning before

$$\epsilon'_2 = \epsilon_b + \frac{2\rho_S \epsilon_s}{R \rho_V}, \quad (\text{S35})$$

note that apart from a different pre-factor, equation S35 is identical to equation S31, i.e. the energetic term  $\epsilon'_2$  scales inversely with the radius of curvature of the nanopore,  $R$ . However, the numerical scale is different compared with the slit-like pores above.

## References

- [1] Heather Au, Hande Alptekin, Anders C. S. Jensen, Emilia Olsson, Christopher A. O’Keefe, Thomas Smith, Maria Crespo-Ribadeneyra, Thomas F. Headen, Clare P. Grey, Qiong Cai, Alan J. Drew, and Maria-Magdalena Titirici. A revised mechanistic model for sodium insertion in hard carbons. *Energy Environ. Sci.*, 13:3469–3479, 2020.
- [2] R. Väli, A. Jänes, and E. Lust. Alkali-metal insertion processes on nanospheric hard carbon electrodes: An electrochemical impedance spectroscopy study. *Journal of The Electrochemical Society*, 164(11):E3429, jun 2017.
- [3] Michael Peter Mercer, Sam Affleck, Edgardo Maximiliano Gavilán-Arriazu, Alana Aragón Zülke, Philip A. Maughan, Shivam Trivedi, Maximilian Fichtner, Anji Reddy Munnangi, Ezequiel P. M. Leiva, and Harry Ernst Hoster. Sodiation of hard carbon: How separating enthalpy and entropy contributions can find transitions hidden in the voltage profile. *ChemPhysChem*, 23(5):e202100748, 2022.
- [4] J. R. Dahn, J. N. Reimers, A. K. Sleight, and T. Tiedje. Density of states in graphite from electrochemical measurements on  $\text{Li}_x(\text{C}_{1-z}\text{B}_z)_6$ . *Phys. Rev. B*, 45:3773–3777, 1992.
- [5] Michael P. Mercer, Manuel Otero, Miriam Ferrer-Huerta, Agustin Sigal, Daniel E. Barraco, Harry E. Hoster, and Ezequiel P.M. Leiva. Transitions of lithium occupation in graphite: A physically informed model in the dilute lithium occupation limit supported by electrochemical and thermodynamic measurements. *Electrochim. Acta*, 324:134774, 2019.
- [6] Holger Euchner, Bhaghavathi P. Vinayan, M. Anji Reddy, Maximilian Fichtner, and Axel Groß. Alkali metal insertion into hard carbon – the full picture. *J. Mater. Chem. A*, 8:14205–14213, 2020.
- [7] Joshua M. Stratford, Phoebe K. Allan, Oliver Pecher, Philip A. Chater, and Clare P. Grey. Mechanistic insights into sodium storage in hard carbon anodes using local structure probes. *Chem. Commun.*, 52:12430–12433, 2016.
- [8] Julia S. Weaving, Alvin Lim, Jason Millichamp, Tobias P. Neville, Daniela Ledwoch, Emma Kendrick, Paul F. McMillan, Paul R. Shearing, Christopher A. Howard, and Dan J.L. Brett. Elucidating the sodiation mechanism in hard carbon by operando raman spectroscopy. *ACS Appl. Energy Mater.*, 3:7474–7484, 2020.
- [9] Zhaohua Wang, Xin Feng, Ying Bai, Haoyi Yang, Ruiqi Dong, Xinran Wang, Huajie Xu, Qiyu Wang, Hong Li, Hongcai Gao, and Chuan Wu. Probing the Energy Storage Mechanism of Quasi-Metallic Na in Hard Carbon for Sodium-Ion Batteries. *Adv. Energy Mater.*, 11:2003854, 2021.
- [10] Clement Bommier, Xiulei Ji, and P. Alex Greaney. Electrochemical properties and theoretical capacity for sodium storage in hard carbon: Insights from first principles calculations. *Chem. Mater.*, 31:658–677, 2019.
- [11] Kimal Chandula Wasalathilake, Godwin A. Ayoko, and Cheng Yan. Effects of heteroatom doping on the performance of graphene in sodium-ion batteries: A density functional theory investigation. *Carbon*, 140:276–285, 2018.
- [12] E. M. Gavilán-Arriazu, J. M. Hümöller, O. A. Pinto, B. A. López de Mishima, E. P. M. Leiva, and O. A. Oviedo. Fractional and integer stages of lithium ion–graphite systems: the role of electrostatic and elastic contributions. *Phys. Chem. Chem. Phys.*, 22:16174–16183, 2020.
- [13] Joshua M. Stratford, Annette K. Kleppe, Dean S. Keeble, Philip A. Chater, Seyyed Shayan Meysami, Christopher J. Wright, Jerry Barker, Maria-Magdalena Titirici, Phoebe K. Allan, and Clare P. Grey. Correlating local structure and sodium storage in hard carbon anodes: Insights from pair distribution function analysis and solid-state nmr. *J. Am. Chem. Soc.*, 143:14274–14286, 2021.